Indian Journal of Pure & Applied Physics
Vol. 63, August 2025, pp. 684-691
DOI: 10.56042/ijpap.v63i8.17176

Variation of Structural, Optical, and Electrical properties of CuAl-SnO_2/Ag/CuAl-SnO_2 with Ag Layer Thickness

Anju Dutt[a,b,*], Harpreet Singh[a,b], Sangeeta[a,b], Sandeep Grover[a,b] & Anand Kumar[b]

[a]Department of Physics, Kurukshetra University, Kurukshetra 136 119, India

[a]Department of Physics, Institute of Integrated and Honour Studies, Kurukshetra University, Kurukshetra 136 119, India

Received: 17 Feb 2025; accepted:4 July 2025

The present work reports the effect of sandwiched layer thickness on the structural, electrical, and optical properties of the (Cu, Al)-SnO_2/Ag/(Cu, Al)-SnO_2 (CAT/Ag/CAT) structures deposited by the E-beam evaporation technique on the glass substrate. The morphology of the Ag layer with increasing thickness affects the electrical and optical properties of the multilayer structure. The formation of Ag islands is confirmed by Field Emission Scanning Electron Microscope (FESEM) techniques, which follow the Volmer-Weber island growth mechanism. The multilayer structure with a 16 nm Ag thickness exhibits the highest transmittance and lowest resistivity, i.e., 84.75% and 3.24×10^{-5} Ω-cm, respectively. The Hackke figure of merit is calculated, and the CAT/Ag(16 nm)/CAT multilayer structure shows the best figure of merit of 4.48×10^{-2} Ω^{-1}.

Keywords: Transparent Conducting Oxide, Multilayer structure, Sandwich layer thickness, Morphology, Optoelectronics applications

1 Introduction

Transparent Conducting Oxides (TCOs) are known for simultaneously showing high conductivity and high transparency. These properties make TCO crucial for various optoelectronic devices, including thin-film solar cells[1,2], light-emitting diodes (LEDs)[3], flat-panel displays[4], transparent heaters[5,6], and Electrochromic windows[7]. Achieving both low resistivity and high transparency in intrinsic stoichiometric TCO materials is challenging. While Indium-doped Tin Oxide (ITO) is commonly used as a transparent conductor, it has several drawbacks, including low abundance, toxicity, poor mechanical properties, and high cost. Consequently, there is a need to develop alternative materials that are more suitable for optoelectronic devices. Tin Oxide (SnO_2) is an n-type transparent oxide semiconductor with a direct and wide bandgap (3.6 eV) and exhibits high transmittance in the visible light region; therefore, it offers significant potential for optoelectronic applications[4-7]. Doped and co-doped transparent conductors are emerging as viable solutions to improve the properties of TCO in optoelectronic applications.

Multilayer structures of TCOs have gained researchers' interest because they exhibit better properties, such as lower resistivity and higher transmittance, as compared to single-layer films. Recent studies on doped multilayer structures, including Al-SnO_2/Ag/Al-SnO_2[8], Ga-SnO_2/Cu/Ga-SnO_2[9], ITO/Ag/ITO[10], Nb-SnO_2/Ag/Nb-SnO_2[11], ZTO/Ag/ZTO[12], have shown enhanced properties. Then, researchers have been concerned about further improving their properties while developing codoped TCO multilayer structures. Some codoped multilayer structures and single-layer TCO thin films have been explored such as IZTO/Ag/IZTO[13], IGZO/Ag/IGZO[14], GAZO/Ag/GAZO[15], $CuCrMgO_2$/Ag/$CuCrMgO_2$[16], Barium and Antimony doped SnO_2 thin film[17], Al and Ni doped SnO_2[18], In and Co doped tin oxide thin film[19], etc. The Ag metal is typically used as a mid-layer in multilayer thin films due to its low resistivity and high transmittance in the optical region at low thickness[19]. Various techniques are available for developing multilayer structures, including RF sputtering[20], thermal evaporation[21], pulsed laser deposition (PLD) [22,23], the sol-gel method[24], and atomic layer deposition (ALD)[25], etc. The e-beam evaporation method is low-cost, easily operated, and suitable for making thin films.

In the present study, the author aims to combine Cu and Al as co-doped materials in SnO2, aiming to achieve good electrical and optical properties simultaneously. The Cu and Al have their low cost and are easily available. The silver metal (Ag) is used

*Corresponding author: E-mail:anju.iihs@kuk.ac.in

as a sandwich layer. The effect of Ag layer thickness on the structural, electrical, and optical properties of co-doped multilayer structure (Cu-Al)-SnO_2/Ag/(Cu-Al)-SnO_2 deposited by the E-beam evaporation method on a glass substrate is discussed in detail. This multilayer structure has been named as CAT/Ag/CAT, for simplicity.

2 Materials and Methods

Glass slides measuring 1.5 cm × 1.5 cm were used as substrates. The glass substrates were cleaned ultrasonically with distilled water, acetone, and isopropyl alcohol for 10 minutes each. Thereafter, the substrates were dried in an oven at 120℃. The CAT/Ag/CAT multilayer thin films were successfully deposited by the E-Beam Evaporation method.

Initially, the CAT targets were prepared by the solid-state reaction method for thin film deposition. In this method, 2 mol% of Cu and 2 mol% of Al were mixed in 96 mol% of tin oxide powder and grinded in a mortar pestle for 2 hrs. The powder was pelletized in a hydraulic machine at a 50 kg/cm^2 pressure. The CAT pellets were sintered at 950℃ for 2 hr. The commercially available pure Ag metal chunks and CAT pellets were used as target material. The controlling deposition parameters for the CAT and Ag layers deposited in an E-beam evaporation chamber are shown in Table 1.

The thickness of the layers was monitored by a quartz crystal thickness monitor placed in the evaporation chamber. In this work, we fixed the top and bottom CAT layer thickness to 30 nm and varied the mid-Ag layer thickness to 8 nm, 12 nm, 16 nm, and 20 nm. The CAT/Ag(8 nm)/CAT, CAT/Ag (12 nm)/CAT, CAT/Ag(16 nm)/CAT and CAT/Ag (20 nm)/CAT multilayers were denoted as CAT1, CAT2, CAT3 and CAT4 respectively.

2.1 Characterization Techniques

The structural properties were investigated using the X-ray diffraction (XRD) Technique (Bruker D8 Advance X-ray Diffractometer) at a glancing angle of 0.5°. Optical characterization was performed using UV-visible spectroscopy (UV 3600 Plus Shimadzu UV-VIS-NIR spectrophotometer). Surface morphology was studied with Field Emission Scanning Electron Microscopy (JSM-7610FPlus), and particle size was examined using ImageJ software. Surface topography was studied using Atomic Force Microscopy (AFM) (Bruker Multimode-8 AFM), and the analysis was performed with Nanoscope Analysis 1.8 software. Electrical properties were investigated using the Hall effect measurement technique with a 0.5 Gauss magnetic field in the Van der Pauw configuration, and the results were analyzed with Ecopia software.

3 Results and Discussion

The XRD spectra recorded for CAT1, CAT2, CAT3, and CAT4 are depicted in Fig. 1, which shows the crystalline nature of the multilayer structure.

The Ag peaks are observed at various 2θ angles, i.e. 38.29°, 44.24°, 64.60°, and 77.47°, 81.82° representing (111), (200), (220), (311), and (222) planes, respectively (COD card no:00-150-9145)[26]and SnO_2

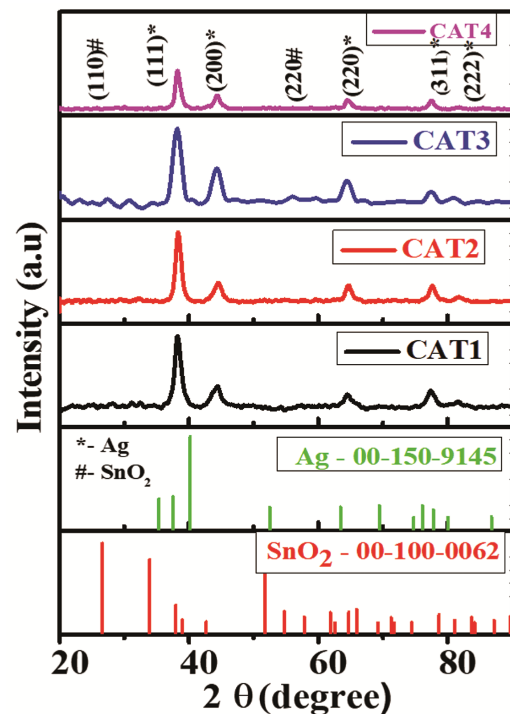

Fig. 1 — X-ray diffraction pattern of CAT1, CAT2, CAT3, and CAT4

Table 1 — Deposition parameters of the CAT/Ag/CAT structure

Deposition of layer	Vacuum Pressure (mbar)	Deposition Rate (Ang./sec)	Substrate rotation (rpm)	Voltage (KV)	Current (mA)	Temp. (℃)
CAT	2×10^{-5}	0.3	10	5	40	200
Ag	2×10^{-5}	0.3	10	5	7	30
CAT	2×10^{-5}	0.3	10	5	40	200

peak shown at 27.4° corresponds to (110) (COD Card no: 00-100-0062)[27] confirms the polycrystalline nature of multilayer films. The average crystallite size (D) was calculated by using the Debye-Scherrer equation[28]:

$$D = K\lambda/\beta cos\theta \quad \ldots(1)$$

Where K is the Scherrer Constant, and its value is 0.9, λ is the wavelength (nm) of the incident Cu K_α X-rays, β is the Full Width Half Maxima (FWHM) of the diffraction peaks, and θ is the diffraction angle in radians. The average crystallite size is found to be 4.7 nm, 7.5 nm, 6.6 nm, and 8 nm for CAT1, CAT2, CAT3, and CAT4 samples, respectively.

Figure 2 presents the transmittance spectra of all multilayer samples in the UV-visible region. The optical analysis reveals that the transmittance behavior of the thin films is strongly dependent on the Ag layer thickness. All samples exhibit maximum transmittance within the 400–500 nm wavelength range, with specific transmittance values (T) for samples CAT1, CAT2, CAT3, and CAT4 detailed in Table 2.

The transmittance peak demonstrates a distinctive shift pattern: it shifts toward higher wavelengths as the Ag thickness increases from 8 nm to 16 nm, then shifts back to lower wavelengths when the Ag thickness reaches 20 nm. Notably, the transmittance increases from 63.99% to 71.04% as the Ag layer thickness grows from 8 nm to 12 nm. This behavior can be attributed to the island growth mechanism

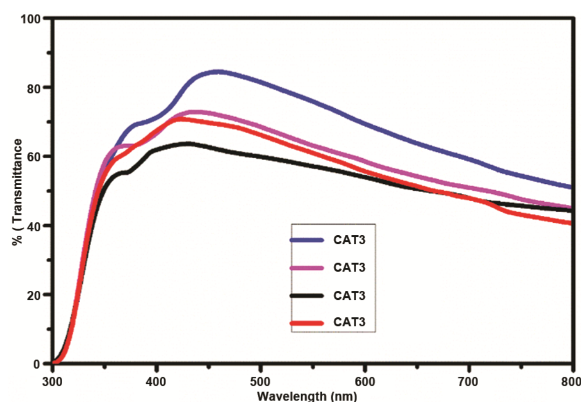

Fig. 2 — Transmittance vs Wavelength Curve for CAT1, CAT2, CAT3, and CAT4

Table 2 — Value of transmittance of CAT1, CAT2, CAT3, and CAT4.

S. No.	Sample Name	% Transmittance
1	CAT1	63.99
2	CAT2	71.04
3	CAT3	84.75
4	CAT4	73.14

during the early stages of thin film formation. Initially, at 8 nm Ag thickness, metal nuclei develop into disconnected islands[13]. These isolated islands because significant light scattering, resulting in the lowest observed transmittance. As the Ag layer thickness increases to 12 nm, these islands begin to interconnect, leading to improved transmittance values.The formation of a continuous layer occurs at 16 nm Ag thickness, yielding the maximum transmittance of 84.75%. This finding correlates well with the FESEM results presented in Fig. 3. However, at 20 nm Ag layer thickness, a hypsochromic shift in transmittance occurs, accompanied by a decrease in transmittance to 73.14%. This reduction is attributed to the surface plasmon resonance (SPR) effect[29] and enhanced reflection from the continuous Ag metallic surface, which becomes more pronounced at increased thickness.

The FESEM micrographs of multilayer CAT/Ag/CAT structures are depicted in Fig. 3. The FESEM result reveals that the morphology of the multilayer thin film changes with varying Ag layer thickness. These micrographs demonstrate the formation of circular-shaped Ag islands. At 8 nm thickness, the islands are discrete and spaced apart. As the Ag layer thickness increases from 8 nm to 12 nm, the island density rises, and they begin to merge. By 16 nm, a continuous Ag layer is formed.

Figure 4 shows the elemental composition (EDS spectra) of the CAT3 sample, as detailed in Table 3, confirming the presence of Sn, O, Al, Cu, and Ag. The oxygen stoichiometry validates the oxidation of Sn.

The FESEM cross-sectional image of CAT4, revealed in Fig. 5, confirms the deposition of the sandwich layer between two metal-oxide layers. The approximate thickness (30 nm ± 3 nm/ 20 nm ± 1 nm/ 30 nm ± 4 nm) of the multilayer structures was estimated using Image J software.

Figure 6 shows the effect of variation in Ag layer thickness on the electrical properties of the CAT/Ag/CAT multilayer structures. It is observed that with an increase in Ag thickness from 8 nm to 16 nm, the resistivity and sheet resistance of the multilayer thin films show similar variation trends.

The resistivity and sheet resistance decrease from 110 × 10^{-5} to 3.24 × 10^{-5} Ω-cm and 161 to 4.26 Ω/sq, respectively, for Ag thickness variation from 8 nm to 16 nm. At 20 nm Ag thickness, resistivity and sheet resistance increase to 4.81 × 10^{-5} Ω-cm, and 6.01 Ω/sq, respectively.

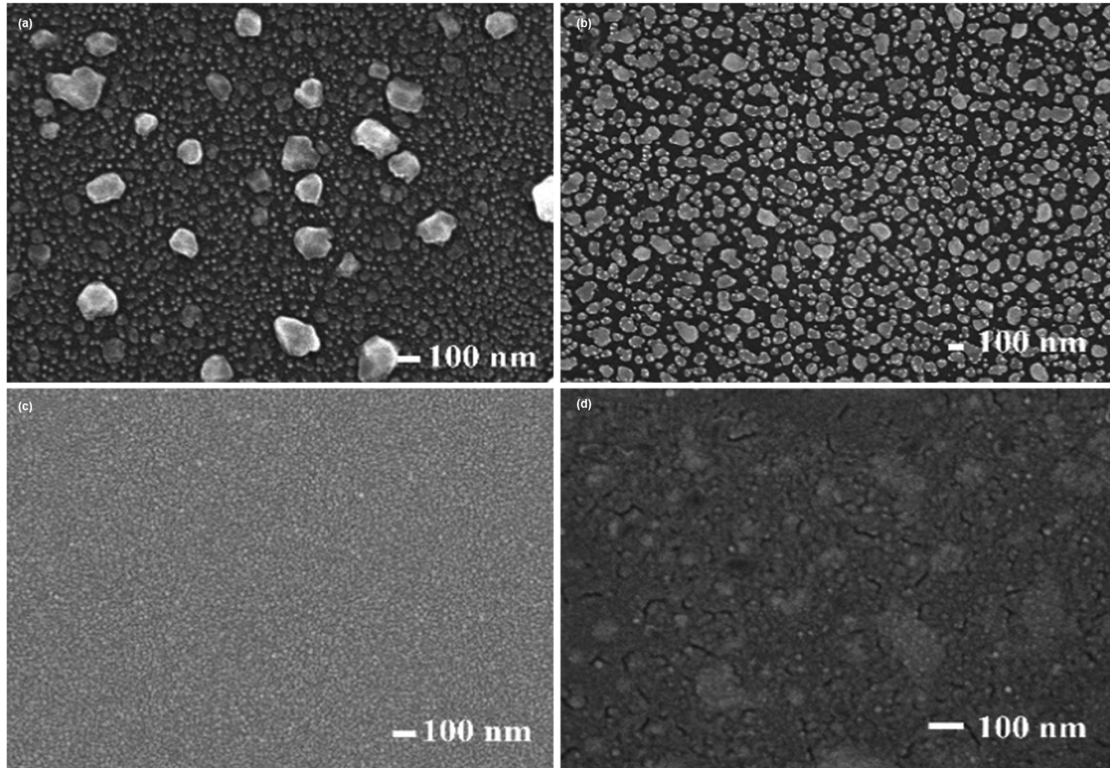

Fig. 3 — FESEM images of CAT/Ag in which Ag layer thickness varies from (a) 8nm (b) 12nm (c) 16nm and (d) 20nm

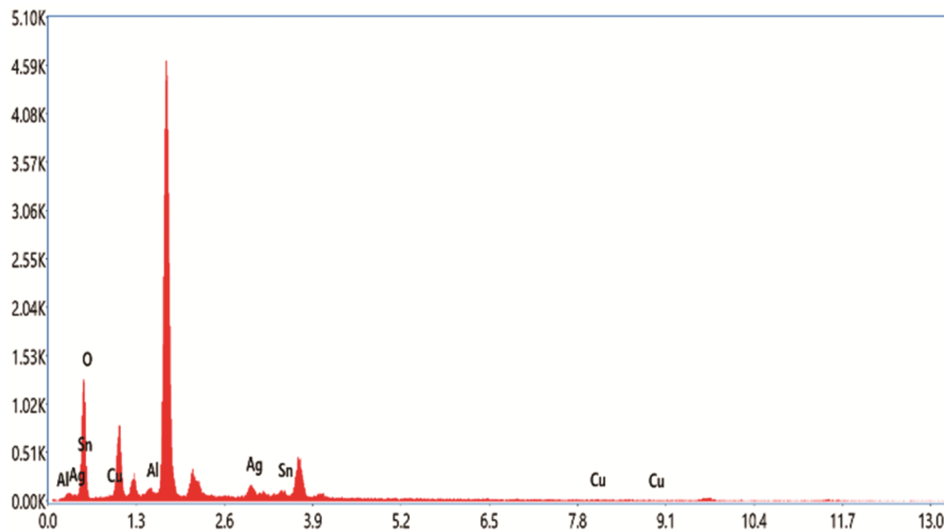

Fig. 4 — EDS spectra of CAT3

Table 3 — Weight percentage of elements in the CAT/Ag/CAT structure

S. no.	Elements	Weight %
1	O	77.4
2	Al	3.3
3	Cu	2.2
4	Ag	9.9
5	Sn	7.4

The sheet resistance of 4.26 Ω/sq and the resistivity of 3.24×10^{-5} Ω-cm obtained at 16 nm thickness demonstrate concordance with the results reported in Guillean et al[30]. The hall mobility and carrier concentration rise from 0.357 to 10.2 cm^2/V-s and 1.6×10^{22} to 1.88×10^{22} cm^3, respectively, with an increase in Ag thickness from 8 nm to 16 nm, as

shown in Table 4. At 20 nm, the mobility and carrier concentration of the thin film decrease to 5.99 cm^2/V-s and 2.17×10^{22} cm^3, respectively.

The work function of the metal oxides is larger than that of metals before contact[31], as shown in Fig. 7. Ohmic contacts form at the interface between the metal and metal oxide semiconductors. At thermodynamic equilibrium, when the Fermi levels of both layers merge, carrier electrons migrate from Ag to the CAT layer (from low work function to high work function), consistent with Schottky's theory[32]. This carrier transfer mechanism explains the enhanced carrier concentration and mobility. All samples exhibit n-type semiconducting behavior, as negative Hall coefficients are observed for all samples. A significant factor is the morphology of the Ag layer, which influences the performance of the multilayer thin film. The conduction mode can be described by the island growth mechanism of the Volmer-Weber model, as the glass substrate is amorphous.

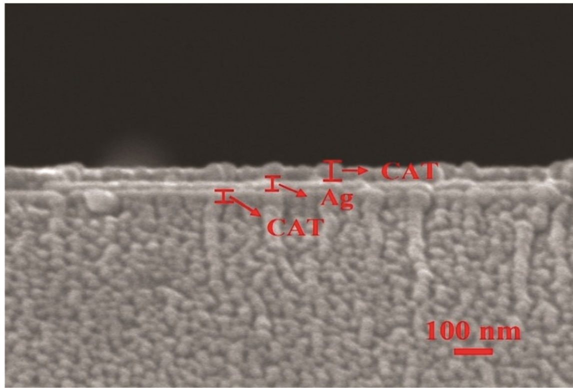

Fig. 5 — FESEM cross-sectional image of CAT4

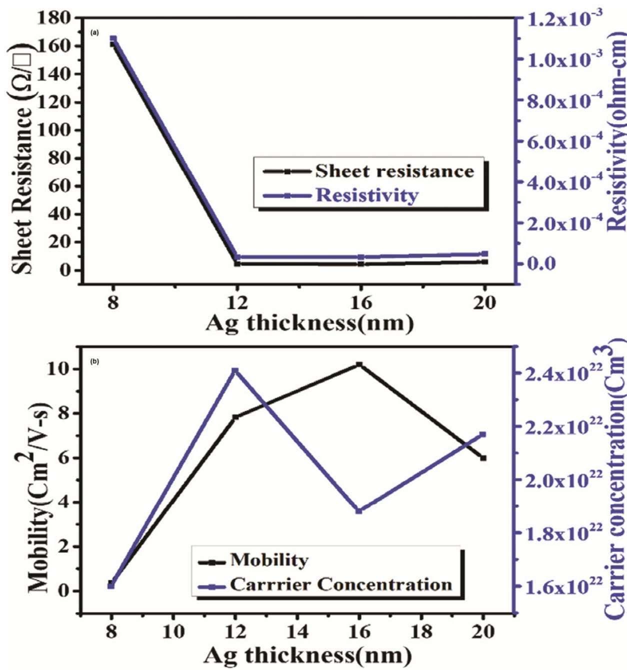

Fig. 6 — (a) Sheet resistance and Resistivity as a function of Ag thickness of CAT/Ag/CAT multilayer thin films, (b) Carrier concentration and mobility as a function of Ag thickness of CAT/Ag/CAT multilayer thin films

A schematic diagram of the growth stages of the Ag film and the process of carrier transport with Ag thickness is shown in Fig. 8. At the early growth stages of the Ag film, specifically at thicknesses of 8 nm and 12 nm, discrete and disconnected islands form, as depicted in Fig. 8(a), where conduction through metal oxides dominates. As the Ag layer grows to a thickness of 16 nm, it forms a continuous layer, as illustrated in Fig. 8(b), which is also evident from the FESEM results. The conduction mode in discontinuous islands with small gaps is quantum tunneling[31,33,34]. As the islands grow further, the gaps between them disappear, forming a connected metal network structure through which conduction occurs,

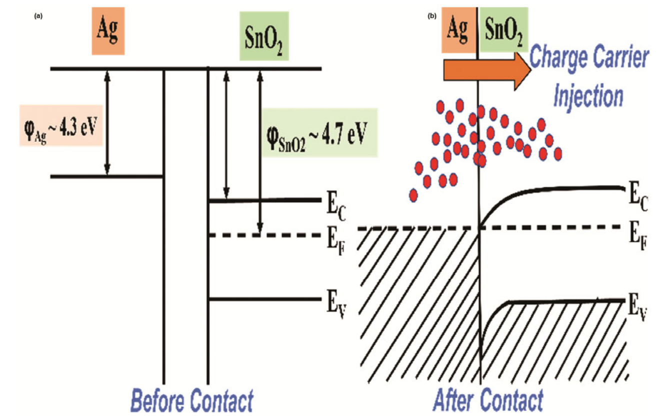

Fig. 7 — Schematic energy band diagram of Ag and SnO_2 layers (a) Before Contact, (b) After Contact

Table 4 — Values of electrical parameters of CAT1, CAT2, CAT3, and CAT4

Sample name	Sheet res. (Ω/sq.)	Resistivity (Ω-cm)×10^{-5}	Mobility (Cm^2/V-s)	Conductivity (Ω^{-1} cm^{-1})	Carrier Conc. (/ $cm^3 \times 10^{22}$)	Hall Coeff. (cm^3/C×10^{-4})
CAT1	161	110	0.357	911	1.6	-3.91
CAT2	4.59	3.31	7.82	30200	2.41	-2.59
CAT3	4.26	3.24	10.2	30900	1.88	-3.32
CAT4	6.01	4.81	5.99	20800	2.17	-2.88

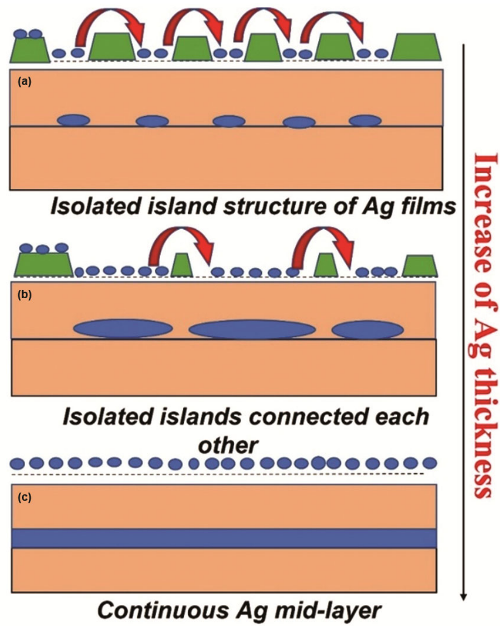

Fig. 8 — Schematic of the growth stage of Ag film and Carrier transport with Ag layer thickness

as shown in Fig. 8(c). This explains the increase in conductivity of the CAT/Ag/CAT multilayer structure with the increase in Ag layer thickness.

The topography of the CAT1, CAT2, CAT3, and CAT4 samples has been studied and AFM 3D images are shown in Fig. 9. The RMS surface roughness, Average surface roughness, and particlesize were measured using Nanoscope Analysis 1.8software. All the multilayer structures exhibit a smooth morphology. The RMS surface roughness of the multilayer thin film decreases from 3.52 nm to 1.11 nm as the Ag layer thickness increases from 8 nm to 16 nm. However, at 20 nm Ag thickness, the surface roughness increases to 3.37 nm, with the average surface roughness reflecting the same variation trends with Ag thickness, as shown in Table 5. This can be attributed to the fact that, at 8 nm Ag thickness, there are disconnected islands, resulting in high surface roughness. An increase in island density occurs with reduced gaps as the thickness increases. A continuous film formed at 16 nm Ag thickness corresponds to

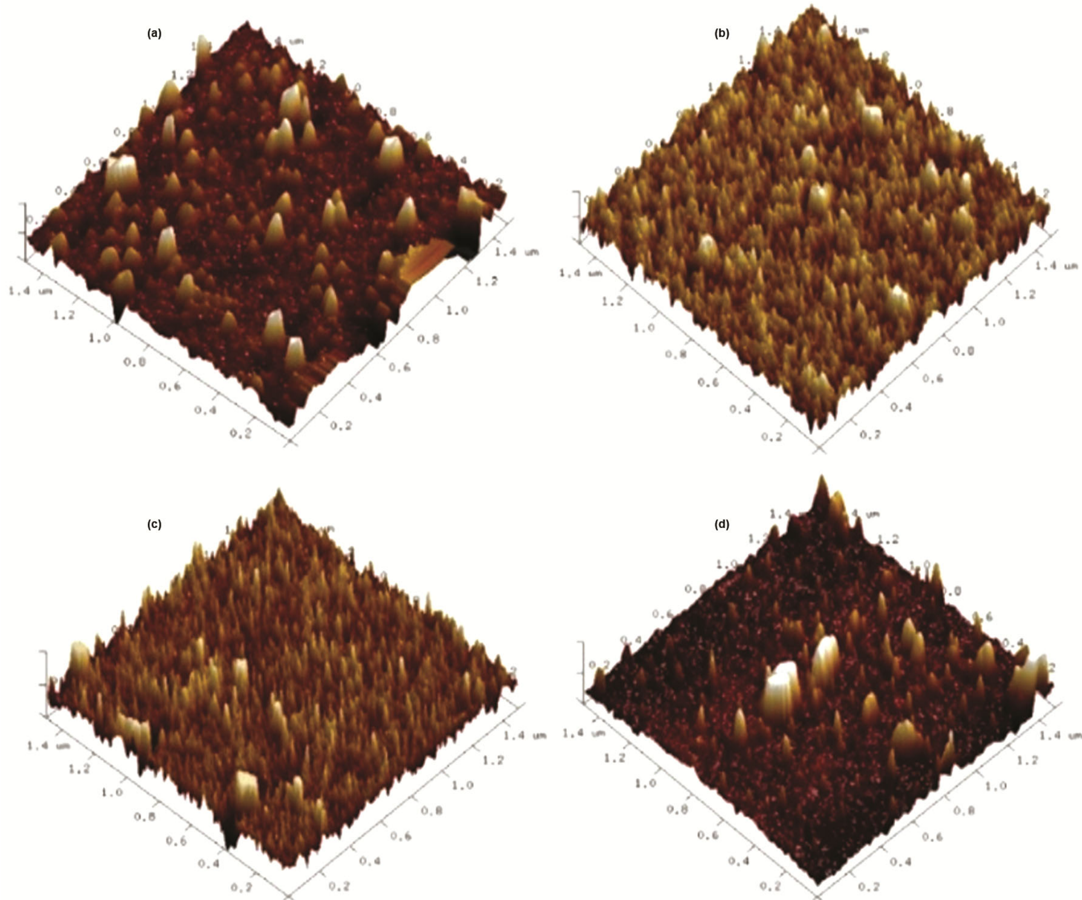

Fig. 9 — AFM 3D images of (a) CAT1 (b) CAT2 (c) CAT3, and (d) CAT4

Table 5 — Calculated values of surface roughness and particle size in the nm range

S. No.	Sample name	RMS Surface roughness (nm)	Average Roughness (nm)	Particle size(nm)
1.	CAT 1	3.52	2.35	55.80
2.	CAT 2	1.30	1.01	55.64
3.	CAT 3	1.11	0.87	52.08
4.	CAT4	3.37	2.19	55.05

Table 6 — Figure of merit of CAT1, CAT2, CAT3, CAT4

S. no.	Sample Name	Figure of Merit $(\text{ohm})^{-1}$
1	CAT1	7.15×10^{-5}
2	CAT2	7.13×10^{-3}
3	CAT3	4.48×10^{-2}
4	CAT4	7.29×10^{-3}

lower roughness. The upper CAT layer is deposited with varying smoothness depending on the continuity of the Ag layer beneath, leading to differing surface roughness as measured by AFM. The surface roughness parameter also affects the change in the transmittance of the film. The larger the surface roughness, the greater the scattering of incident light from the film surface, resulting in lower transmittance.

The particle size, calculated using Nanoscope Analysis 1.8 software, is found to be almost the same for all the samples, as shown in Table 5.

The figure of merit (FOM) is a crucial parameter for evaluating the quality of transparent conducting films and assessing the overall efficiency of multilayer configurations. This metric provides a quantitative assessment by incorporating two fundamental parameters: sheet resistance and optical transmittance. The FOM serves as an essential tool for determining the effectiveness and measuring the performance of transparent conducting films. Researchers Fraser & Cook[35], along with Haacke, have developed various formulas to evaluate the quality of transparent conducting films. Haacke's formula[36] for calculating the FOM is expressed as:

$$\Phi = (T)^{10}/R_{sh} \quad \ldots (2)$$

Here, T is the average transmittance, and R_{sh} is the sheet resistance of the multilayer thin film. Table 6 shows the calculated FOM values of CAT1, CAT2, CAT3, and CAT4.It is noted that with increasing Ag thickness from 8 nm to 12 nm, FOM increases from $7.15 \times 10^{-5}\ \Omega^{-1}$ to $7.13 \times 10^{-3}\ \Omega^{-1}$. At 16 nm Ag thickness, it shows the best figure of merit, i.e., $4.48 \times 10^{-2}\ \Omega^{-1}$. After that, the figure of merit decreases to $7.29 \times 10^{-3}\ \Omega^{-1}$ at 20 nm Ag thickness.

4 Conclusion

The CuAl-SnO_2/Ag/CuAl-SnO_2 multilayer thin films were successfully deposited on glass substrates using the electron beam evaporation synthesis method. Grazing incidence X-ray diffraction (GXRD) analysis confirmed the polycrystalline nature of the multilayer films, with diffraction patterns matching the Crystallographic Open Database (COD) card files. The calculated crystallite sizes ranged from 4 to 8 nm. Field emission scanning electron microscopy (FESEM) confirmed island formation of the metal layer within the multilayer structure. The morphology of the intermediate Ag layer played a crucial role in enhancing both the electrical and optical properties of the multilayer configuration. Atomic force microscopy (AFM) results demonstrated a strong correlation with the optical properties, which were consistent with UV-visible spectroscopy findings. The conductivity mechanism was successfully explained through the island growth mechanism based on the Volmer-Weber model. The analysis revealed that different conduction mechanisms dominate depending on the specific stages of island growth, as comprehensively detailed in this study. The charge carrier migration at interfaces within the multilayer configuration was elucidated using energy band diagrams. At a critical Ag thickness of 16 nm, the multilayer structure exhibited continuous layer formation, resulting in the highest optical transmittance and superior electrical conductivity compared to other investigated thicknesses (8 nm, 12 nm, and 20 nm).The optimal figure of merit of $4.48 \times 10^{-2}\ \Omega^{-1}$ was achieved at 16 nm Ag thickness, demonstrating the superior performance of this multilayer thin film configuration.

Acknowledgment

The author thanks the Ion Beam Centre at Kurukshetra University, Kurukshetra, for providing the AFM and UV facilities. The author also acknowledges the Central Instrumentation Laboratory at Guru Jambheshwar University, Hisar, for the FESEM and XRD facilities. Additionally, thanks are extended to MNIT, Jaipur, for the e-beam synthesis facilities and Hall effect measurements.

References

1 O'regan B &Grätzel M *Nature*, 353 (1991), 737.
2 Kim H, Kushto G P, Arnold C B, Kafafi Z H & Piqué A, *Appl Phys Letters*, 85 (2004) 464.
3 Brütting W, Meier M, Herold M, Karg S & Schwoerer, *Chemphys*, 227 (1998) 243.
4 Fukano T, Motohiro T, Ida T & Hashizume H, *J Appl Phys*, 97 (2005) 084314.
5 Yu S, Liu X, Dong H, Wang X & Li L, *Ceram Int*, 47 (2021) 20379.
6 Kim D H, Cho K S & Kim H K, *Sci rep*, 7 (2017) 2550.

7 Kim K H, Koo B R & Ahn H J, *Ceram Int*, 45 (2019) 15990.
8 Kim J H, Moon Y J, Kim S K, Yoo Y Z & Seong T Y, *Ceram Int*, 41 (2015) 14805.
9 Gong L, Lu J & Ye Z, *Thin Solid Films*, 519 (2011) 3870.
10 Jeong J A & Kim H K, *Sol Energy Mater Sol Cells*, 93 (2009) 1801.
11 Dhar A & Alford T L, *J Appl Phys*, 112 (2012) 103113.
12 Ekmekcioglu M, Erdogan N, Astarlioglu A T, Yigen S, Aygun G, Ozyuzer L & Ozdemir M, *Vacuum*, 187 (2021) 110100.
13 Choi K H, Nam H J, Jeong J A, Cho S W, Kim H K, Kang J W & Cho W, *JAppl Phys Letters*, 92 (2008) 22.
14 Kim J H, Lee H, Na J Y, Kim S K, Yoo Y Z & Seong T Y, *CurrAppl Phys*, 15 (2015) 452.
15 Jung Y S, Kim W J, Choi H W & Kim K H, *Microelectron Eng*, 89 (2012)124.
16 Oh D, No Y S, Kim S Y, Cho W J, Dal Kwack K & Kim T W, *J Alloys Compd*, 509 (2011) 2176.
17 Ramarajan R, Kovendhan M, Thangaraju K, Joseph D P, Babu R R & Elumalai V, *J Alloys Compd*, 823 (2020) 153709.
18 Bouabdalli E M, El Jouad M, Garmim T, Touhtouh S, Louardi A, Monkade M & Hartiti B, *Int J Photoenergy*, *2021* (2021) 5556441.
19 Ameur S B, Barhoumi A, Mimouni R, Amlouk M & Guermazi H, *Superlattices Microstruct*, 84 (2015) 99.
20 Sayeed M A & Rouf H K, *J Mater Res Technol,* 15 (2021) 3409.
21 NajiI S, *Nanoeng Nanosyst* 233 (2019) 17.
22 Kim J P, Lee S A, Bae J S, Park S K, Choi U C & Cho C R, *Thin Solid Films,* 5165223 (2008).
23 Kaur G, Mitra A & Yadav K L, *Prog Nat Sci Mater Int*, 25 (2015) 12.
24 Sharmin A, Tabassum S, Bashar M S & Mahmood Z H, *J Theoretical Appl Phys,* 13 (2019) 123.
25 Lanje A S, Sharma S J & Pode R B, *J Chem Pharm Res*, 2 (3) (2010) 478.
26 Baur W H & Khan A A, *Struct Sci*, 27 (1971) 2133.
27 Novgorodova M I, Gorshkov A I & Mokhov A V, *Int Geo Rev*, 23 (1981) 485.
28 Patterson A L, *Phys Rev,* 56 (1939) 978.
29 Temple T L, Mahanama G D K, Reehal H S & Bagnall D M, *Sol Energy Mater Sol Cells*, *93* (2009) 1978.
30 Guillen C & Herrero J, *Thin Solid Films*, 520 (2011) 1.
31 Yu S, Zhang W, Li L, Xu D, Dong H & Jin Y, *Thin Solid Films*, 552 (2014) 150.
32 Tersoff J, *Phys Rev B,* 32 (1985) 6968.
33 Biegański P, Dobierzewska-Mozrzymas E, Pieciul E & Szymczak G, *Vacuum*, 74 (2004) 211.
34 Singh R, Gupta M & Mukherjee S, *J Mater Sci Mater Electron*, 33 (2022) 6942.
35 Cisneros-Contreras I R, Muñoz-Rosas A L & Rodríguez-Gómez, *Results Phys*, 15 (2019) 102695.
36 Haacke G, *J Appl Phys,* 47 (1976) 4086.